19th International Conference on
Adaptive Structures and Technologies
October 6-9, 2008
Ascona, Switzerland

H_∞ Control for Reducing Cross-coupling in a Compliant XY Nanopositioning Stage

Yuen Kuan Yong, Kexiu Liu, and S. O. Reza Moheimani*
School of Electrical Engineering and Computer Science, The University of Newcastle, Callaghan, NSW 2308, Australia.
Email:[Yuenkuan.Yong, Kexiu.Liu, Reza.Moheimani]@newcastle.edu.au
*Corresponsing author, Tel +61249216030, Fax +61249216993

ABSTRACT

A compliant XY nanopositioning platform designed for scanning probe microscopy applications is presented in this article. The device possesses a very high out-of-plane stiffness resulting in extremely low cross-coupling between various axes. However, cross-couplings between X- and Y-axes of the stage cannot be ignored during fast raster scans. A H_∞ controller is designed to minimize cross-coupling between these two axes of the nanoscale positioning stage, particularly at its mechanical resonance frequencies. The controller is augmented with integral action to achieve accurate tracking and damping. Raster scan results over an area of 10μm×10μm with small positioning errors are demonstrated. High-speed accurate raster scans of up to 100Hz, with nanoscale resolution are also illustrated.

Keywords: Nanopositioning stage, Flexure, Cross-coupling, Raster scanning.

1. INTRODUCTION

The invention of atomic force microscope (AFM) in the 1980's [1] has advanced the research studies of materials with demonstrated resolutions up to the atomic level. AFMs utilize sharp probes of few atoms wide (located at the end of a flexible micro-cantilever) and nanopositioning scanners that move samples relative to the probe to perform raster scans over the sample surface. AFM related applications include nano-metrology [2], nano-lithography [3], tracking and analysis of biological cell events [4], nano-patterning and nano-indentation for high-density data storage systems [5]. Piezoelectric tubes with quartered electrodes are widely used as scanners for raster scanning in commercially available AFMs arising from their low cost and ease of installation.

Cross-coupling effects of AFM scanners corrugate scans [6-8] and introduce artifacts to the image which can be mistaken as surface roughness [9]. Various calibration and correction techniques have been developed to reconstruct the distorted AFM images [8, 10]. To avoid the post-processing of scans, a number of approaches have been implemented that minimize the XY-to-Z cross-coupling of piezoelectric tubes [7, 11, 12]. Apart from the XY-to-Z cross-coupling, AFM scanners also possess cross-couplings between their X and Y axes, which can be observed from the experimental data presented in [13]. Atomic force microscopy is often performed at low scanning speeds. At such speeds the adverse effect of cross-coupling between the X and Y axes is insignificant. However, the cross-coupling effect becomes prominent during high-speed scans due to the excitation of mechanical resonances of the scanner. This cross-coupling is known to introduce measurement uncertainties of angles between features in a scan [6].

Compliant, piezoelectric stack-actuated nanopositioning stages have recently been integrated into a small number of commercially available AFMs [14]. Compliant nanopositioning stages can be

designed to have high mechanical resonance frequencies (tens of kHz) and low cross-couplings between various axes (as low as 1%) [15, 16]. As the demand for high-speed, low cross-coupling nanopositioning systems is increasing, particularly in applications of AFM that involve monitoring of fast-pace biological events of cells [17, 18], the use of compliant nanopositioning stages in AFMs has become popular.

A compliant XY nanopositioning stage with low cross-coupling and high resonance frequencies is designed and presented in this article. Unlike a conventional piezoelectric tube scanner, the compliant stage is designed to have only XY-plane motions. The Z scanner is detached from the stage. This XY nanopositioning stage is aimed to be fitted into an AFM system similar to that proposed in [19]. In this AFM, a sample is moved in the XY plane using the planar XY stage while the AFM probe is maneuvered along the Z-axis by the Z scanner (see Figure 1). This design configuration practically removes the XY-to-Z cross-couplings. Furthermore, the dynamic performance of the Z scanner is no longer limited by that of the XY stage. Although the cross-coupling between the X and Y axes of the nanopositioning stage presented in this article is small, the effect is amplified at the resonance frequencies of the stage. To reduce scanning errors, it is common practice to operate the nanopositioning stage at 1/100th of its first mechanical resonance frequency [20], which limits the AFM's scanning speed. Therefore, reducing the cross-coupling of the compliant stage is a pre-requisite of achieving rapid scanning probe microscopy.

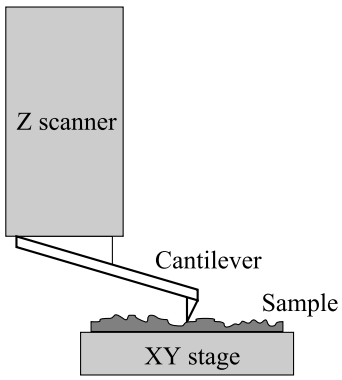

Figure 1. Schematics of an AFM system documented in [19]. Unlike the conventional AFM, the Z scanner is detached from the XY stage in this design.

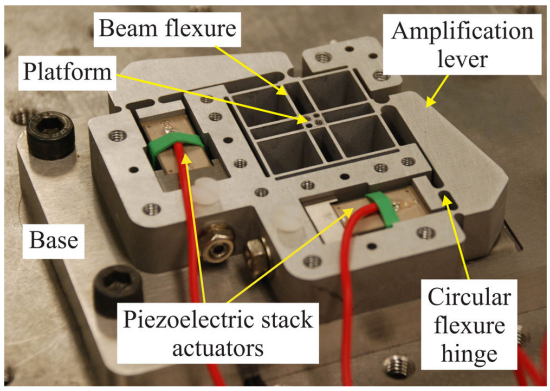

Figure 2. Compliant XY nanopositioning stage. The stage consists of the inner and outer sections. The inner section is designed to minimize the cross-coupling between the X and Y axes. The outer section is designed to amplify the displacement of piezoelectric stack actuators.

In this article, the X-Y cross-coupling of a prototype nanopositioning stage is minimized by (a) mechanically decoupling the two axes through the design of the structure, and (b) implementing a H_∞ controller to reduce the cross-coupling especially during high-speed operations and to achieve accurate tracking performance. The remainder of the paper is organized as follows. The mechanical design and finite-element-analysis (FEA) of the compliant nanopositioning stage are presented in Sec. 2. In Sec. 3, the experimental setup of the nanopositioning system is described. The system identification of the stage is presented in Sec. 4. Sec. 5 discusses the H_∞ controller design and the choice of necessary weighting functions. Experimental closed loop raster scan designs are presented in Sec. 6. Sec. 7 presents the noise characterization of the closed loop system. Finally, Sec. 8 concludes the paper.

2. MECHANICAL DESIGN

The design of the XY nanopositioning stage is based on the concept of compliant mechanisms where the requisite motions are generated through elastic deformations of flexible mechanical elements (flexures). Unlike conventional mechanisms, compliant mechanisms do not have gears, revolute and sliding joints. Consequently, the problems of wear, backlash, friction and the need for

lubrication are eliminated [21, 22]. This provides repeatable and smooth motions necessary for accurate nanoscale positioning. The design is monolithic (machined from a single piece of material) and has a parallel kinematic configuration. A parallel structure provides high mechanical stiffness, high motion accuracy and high resonance frequencies, which makes the stage suitable for high-speed, accurate tracking applications [23]. Two piezoelectric stack actuators are incorporated into the stage, each providing the required input displacement to the X and Y axes respectively. They are used to drive the stage due to their capability of providing large forces, high accelerations and repeatable motions over a very large bandwidth [17].

A key design specification for the nanopositioning stage is to minimize the effect of cross-coupling between the two axes of the device. As shown in Figure 2, the nanopositioning stage consists of two main parts: (a) the inner section which consists of a stage and beam flexures, and (b) the outer part which consists of amplification levers and circular flexures. The inner section is designed to minimize the cross-coupling between the X and Y motions of the stage. At the inner section, the stage is held by four pairs of beam flexures. The flexures are arranged in such a way so that they are rigid along the direction of motion and are flexible in the axis perpendicular to the motion [24]. The FEA simulation of motion along the X-axis, obtained using ANSYS, is shown in Figure 3. At the outer section, an amplification lever is integrated into each axis of the stage to amplify the displacement of the piezoelectric stack actuator. The ANSYS estimation of the amplification ratio is about 2.5. The amplified motions are transferred to the inner section to displace the platform located at the inner section.

The nanopositioning stage was fabricated via the WEDM (wire electrical discharge machining) technique due to its accuracy and precision [25]. Aluminum alloy 7075 with Young's modulus of 72GPa and a thickness of 12.8mm was used to fabricate the stage. The chosen material thickness is large enough to ensure that the out-of-plane motion along the Z-axis is negligible. The final design of the nanopositioning stage is estimated to have its first resonance frequency at 2.5kHz and a cross-coupling of -35dB at both axes.

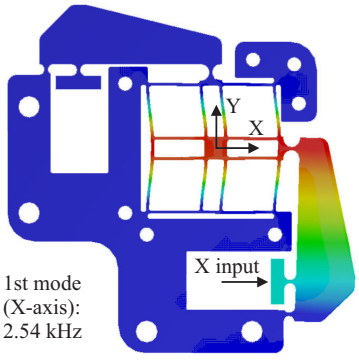

Figure 3. FEA simulation of motions and resonance frequency of the nanopositioning stage along the X-axis. Simulations of the Y-axis are similar.

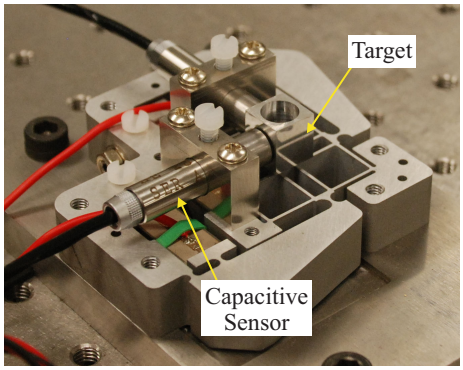

Figure 4. Experimental setup of the nanopositioning stage. The X and Y displacements of the stage are measured using two capacitive sensors. The sensing target is made of aluminum and has a fine surface finish.

3. EXPERIMENTAL SETUP

The nanopositioning stage is mounted on a 10mm steel plate that is rigidly held on an optical table. An aluminum block with a fine surface finish is mounted on the platform of the compliant stage and is used as a target for displacement sensing. It also serves as a stage for the placement of a sample. Two ADE Technologies 8810/2804 capacitive sensors, each with a static gain of 2.5µm/V, are placed adjacent to the aluminium block surfaces to measure the displacement along the X and Y axes (see Figure 4). The two Physik Instrumente piezoelectric stack actuators (P-888.50) are used to generate motions along the two axes. These actuators operate over a voltage range of 0 to 100V and produce a maximum stage motion of 25µm at each axis.

In this work, the nanopositioning stage is used to produce raster scans over a 10μm×10μm area. A triangular waveform and a synchronized staircase signal are generated to produce the raster scans. The triangular and the staircase signals drive the X-axis and Y-axis piezoelectric stack actuators respectively. Hysteresis is the main non-linearity associated with piezoelectric materials. It is known to degrade the trace of the reference signal [26, 27]. Charge actuation has been implemented to substantially reduce the presence of hysteresis in piezoelectric actuators [28-30]. Since the X-axis piezoelectric actuator is driven, repetitively, over a relatively large range (i.e. 10μm), positioning errors due to hysteresis effect at this axis are more significant than that of the Y-axis. A custom-built charge source capable of driving large capacitive loads is employed in this work to reduce the hysteresis effect in the X-axis. The charge amplifier has a gain of 126μC/V and an equivalent voltage gain of 20. The Y-axis piezoelectric stack actuator is driven to trace staircase signals. A voltage amplifier with a gain of -20 was used to drive the Y-axis actuator.

A dSPACE-1005 rapid prototyping system equipped with 16-bit ADC (DS2001) and DAC (DS2102) cards is used to implement a feedback controller in real time. A sampling frequency of 40kHz was chosen to ensure that there were no aliasing effects during the experiments.

4. SYSTEM IDENTIFICATION

The nanopositioning stage is a two-input two-output system. A block diagram is presented in Figure 5 to clarify the associated gains in this system. The X-axis piezoelectric stack actuator was driven by a charge amplifier which has a gain of 126μC/V and an equivalent voltage gain of 20. A voltage amplifier with a gain of -20 was used to drive the Y-axis piezoelectric stack actuators. To identify a linear model of the stage, within the bandwidth of interest, a HP 35670A dual channel spectrum analyzer was used to generate a band-limited random noise input (u_x and u_y) of amplitude 30mVpk within the frequency range of 10Hz to 10kHz. The signals were applied to the X- and Y- axis stack actuators using the charge and voltage amplifiers, respectively. The corresponding capacitive sensor measurements (v_x and v_y) were fed back to the spectrum analyzer to construct the frequency responses of the two channels. The frequency response functions of the system can be described as,

$$\begin{bmatrix} G_{xx}(j\omega) & G_{xy}(j\omega) \\ G_{yx}(j\omega) & G_{yy}(j\omega) \end{bmatrix} = \begin{bmatrix} \dfrac{v_x(j\omega)}{u_x(j\omega)} & \dfrac{v_x(j\omega)}{u_y(j\omega)} \\ \dfrac{v_y(j\omega)}{u_x(j\omega)} & \dfrac{v_y(j\omega)}{u_y(j\omega)} \end{bmatrix} \tag{1}$$

Here, $u_x(j\omega)$, $u_y(j\omega)$, $v_x(j\omega)$, $v_y(j\omega)$ denote the Fourier transforms of u_x, u_y, v_x and v_y respectively.

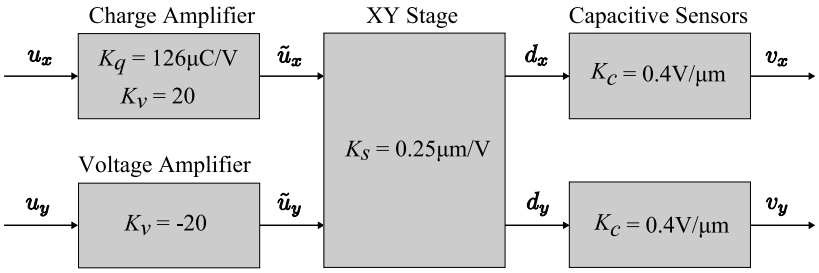

Figure 5. Associated gains of the nanopositioning experimental setup. u_x and u_y are the reference inputs in volts generated by the spectrum analyzer. $\tilde{u}_x$ is the output of the charge amplifier in μC and $\tilde{u}_y$ is the output of the voltage amplifier in volts. d_x and d_y are the actual displacements of the nanopositioning stage in μm, v_x and v_y are the capacitive sensor output in volts. The frequency responses are from input u_x to output v_x and from u_y to v_y.

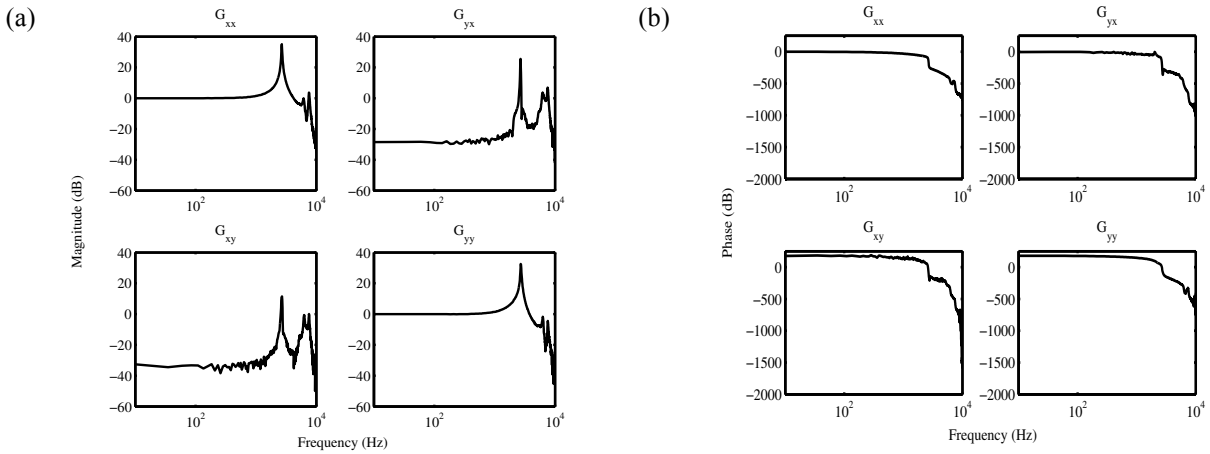

Figure 6. Measured open loop frequency responses of the stage showing (a) magnitude in dB and (b) phase in degree. The inputs are reference voltages u_x and u_y generated by the spectrum analyzer, and the outputs are capacitive sensor voltages v_x and v_y corresponding to displacements d_x and d_y (in μm), as shown in Figure 5. The X-axis piezoelectric stack actuator is driven by a charge amplifier that produces a charge proportional to the reference voltage u_x using a gain of 126 μC/V. The Y-axis piezoelectric stack actuator is driven by a voltage amplifier with a voltage gain of -20.

The measured open loop frequency responses are plotted in Figure 6. The three resonance frequencies occur at 2.7kHz, 6kHz and 7.6kHz. The three resonant peaks of the cross-coupling frequency responses are due to the excitation of mechanical resonance modes at each individual axis.

The open loop scanning performance of the stage is evaluated using raster signals. The nanopositioning stage is used to scan an area of 10μm×10μm. The distance between the consecutive lines is 39nm, providing a total of 256 scan lines along the Y-axis. To evaluate the performance of the proposed high-speed raster scanning arrangement, triangular waves with fundamental frequencies of 40Hz, 60Hz and 100Hz are used to drive the X-axis actuator and the corresponding synchronized staircase signals are used to drive the Y-axis actuator. Figure 7 shows the traces of the triangular and the synchronized staircase signals when the stage is operated in open loop. It can be observed that tracking performance of the nanopositioner when operated in this mode is unacceptably poor.

To appreciate the problem, the desired and the actual trajectories traced by the nanopositioner in the X-Y plane are plotted in Figure 8. It can be observed that as the scan frequency speeds up, the positioning performance of the stage worsens. This is mainly due to the cross-coupling between X and Y axes. The triangular signal used to drive the X-axis stack actuator contains all odd harmonics of the fundamental frequency. The amplitude of these harmonics is attenuated by a factor of $1/n^2$, where n is the number of the harmonic. Despite this, and due to the presence of sharp resonances in the cross-coupling frequency response of the stage, the signal applied to the X-axis corrugates the traced trajectory in the X-Y plane. Another effect that can be observed in Figure 8 is the drift of the traced trajectory. This can be due to creep of the piezoelectric actuators and thermal drift of the stage. Piezoelectric stack actuators embedded into the nanopositioner are uni-polar actuators – to avoid depolarization, only positive voltages can be applied to them. These actuators are biased at 40V, and then AC signals are applied on top of the bias voltage. When operated in this mode, piezoelectric stack actuators are known to creep [31]. Thermal drift is also known to result in a similar drift in nanopositioning platforms [32]. To improve the tracking performance of the system and make it suitable for fast scans, these issues must be addressed. In the next section, we propose a control design framework that achieves this goal.

5. H_∞ CONTROLLER DESIGN

To perform fast and accurate raster scans, a nanopositioning system with high bandwidth, high resolution and good disturbance rejection capabilities is desirable. Previous section clearly illustrated that fast and accurate nanopositioning in open loop is not practical. To achieve accurate and fast nanopositioning, a H_∞ controller was designed and implemented on the system. The controller is

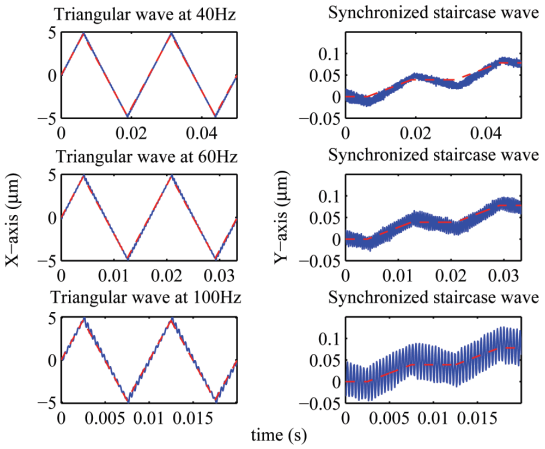

Figure 7. Open loop tracking performance of triangular waves with fundamental frequencies of 40Hz, 60Hz and 100Hz and their corresponding synchronized staircase signals. Reference signals (- -) and output signals (-) are plotted. The resonant mode of the stage is excited by all three signals applied to the X-axis. The excitation effect can be observed at the Y-axis due to the cross-coupling effect.

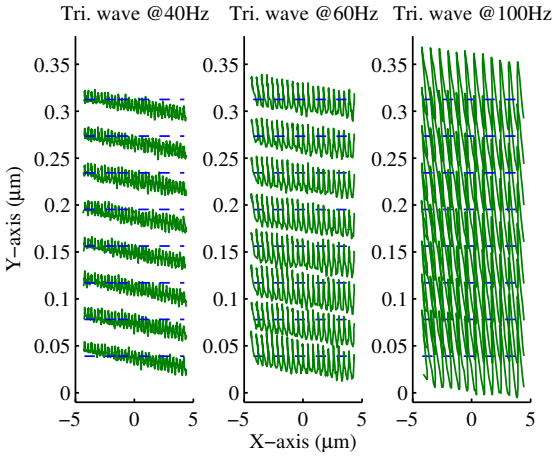

Figure 8. Open loop raster scan results. Reference signals (- -) and output signals (-) are plotted. 90% of the scanning range which corresponds to ±4.5µm along the X-axis is plotted. The scanning lines are 39nm apart. The inclination of scan lines is due to piezoelectric creep and thermal drift of the stage. The resonant mode of the stage is excited due to the triangular signal applied to the X-axis stack actuator and the cross-coupling causes the excitation effect to be seen at the Y-axis.

designed to attenuate the cross-coupling effect between the two axes of the nanopositioner. It also has high gain at low frequencies in order to substantially reduce tracking errors. The controller was also designed to ensure the closed loop system has sufficient bandwidth to perform fast raster scans, i.e. to track fast triangular signals of up to 100Hz in this case.

Figure 9 shows the block diagram of the feedback controlled system with its associated weighting functions. Since the cross-coupling between the two axes is small at low frequencies (see Figure 6), each positioning axis was considered as a SISO system. A controller was designed for each positioning axis and the cross-coupling effect was considered as an additional disturbance to each loop. The control design problem is cast into the standard H_∞ control design framework with the standard structure illustrated in Figure 10. The input disturbance vector is defined as $d = \begin{bmatrix} r & n_d \end{bmatrix}^T$ and the control output vector is defined as $z = \begin{bmatrix} z_1 & z_2 \end{bmatrix}$ where r is the reference signal, n_d is the output disturbance that models the cross-coupling from the Y-axis, u is the control input, z_1 and z_2 are the control outputs. The controller is designed to minimize $\|T_{zd}(s)\|_\infty$, the H_∞-norm of the transfer function from the input disturbance vector to the control output vector.

14^{th} and 12^{th} order plant models were initially identified for the X and Y axes respectively using the subspace based modeling technique [33]. High order plant models lead to high order controllers that could be difficult to implement in real time. Consequently, second order models G_{xx} and G_{yy} of the plant were used for controller design. These transfer functions are described in Eqs. (2) and (3). Figure 11 shows the frequency responses of the measured, the high order and the second order models of the nanopositioning stage. The second order models capture the dynamics of the system up to, and after the first resonance frequency with adequate accuracy.

$$G_{xx}(s) = \frac{1.563s^2 - 3.623\times10^4 s + 4.851\times10^8}{s^2 + 340.4s + 2.84\times10^8} \tag{2}$$

$$G_{yy}(s) = \frac{-1.492s^2 + 3.459\times10^4 s - 4.632\times10^8}{s^2 + 344.3s + 2.905\times10^8} \tag{3}$$

As shown in Figure 11, the reduced order models do not capture the second and the third resonant modes of the stage. For control design purposes the presence of these unmodeled modes is treated as output disturbances to the plant. These resonant modes are small in magnitude, compared with the first resonance of each axis, and appear at high frequencies, above 6kHz. To deal with these out of bandwidth modes the H_∞ controller must be designed to roll-off at high frequencies after the first resonant mode of each axis.

To minimize cross-coupling between the two axes, low order bandpass weighting functions W_{bpx} and W_{bpy} are introduced to X-axis and Y-axis respectively. Each weighting function is tuned to the resonance frequencies of its corresponding axis, as shown in Figure 12. The two weighting functions are,

$$W_{bpx} = \frac{52464.6s}{s^2 + 848.2s + 2.878\times10^8} \times \frac{s^2 + 2133s + 5.54\times10^8}{s^2 + 8796s + 1.934\times10^9} \tag{4}$$

$$W_{bpy} = \frac{48757.6s}{s^2 + 678.6s + 2.878\times10^8} \times \frac{s^2 + 2938s + 7.461\times10^8}{s^2 + 8796s + 1.934\times10^9} \tag{5}$$

The weighting function W_u is introduced to limit the level of control signal applied to each actuator. This is necessary to avoid actuator saturation during the operation of the device in closed loop. This weight was chosen as a constant and it tends to constrain the controller gain at high frequencies. The weighting function W_p is introduced to enforce good tracking performance. Both X and Y axes of the stage have very similar frequency responses. The cross-coupling between the two axes is also very similar. Thus, the same weight W_p was used for both axes, i.e.,

$$W_p = \frac{0.3162s + 6283}{s + 19.87} \tag{6}$$

An integrator was incorporated into the H_∞ controller to achieve a satisfactory tracking of triangular and staircase signals. In Figure 9, this integrator is shown cascaded to the plant. Figure 13 displays frequency responses of the controller designed for each axis, i.e. K_x and K_y.

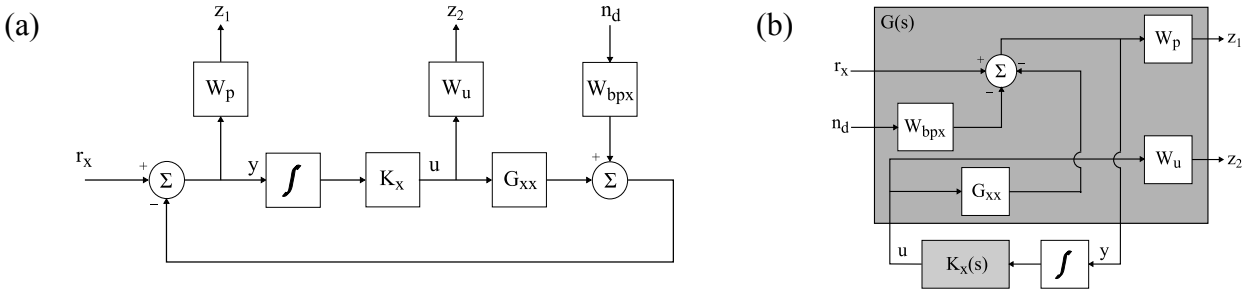

Figure 9. Block diagram of the X-axis feedback loop. Y-axis feedback loop is quite similar. (a) Closed loop system with weighting functions. (b) Equivalent block diagram of the closed loop system which is cast into the H_∞ control design structure.

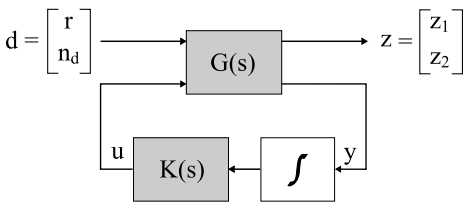

Figure 10. Block diagram of the H_∞ controller.

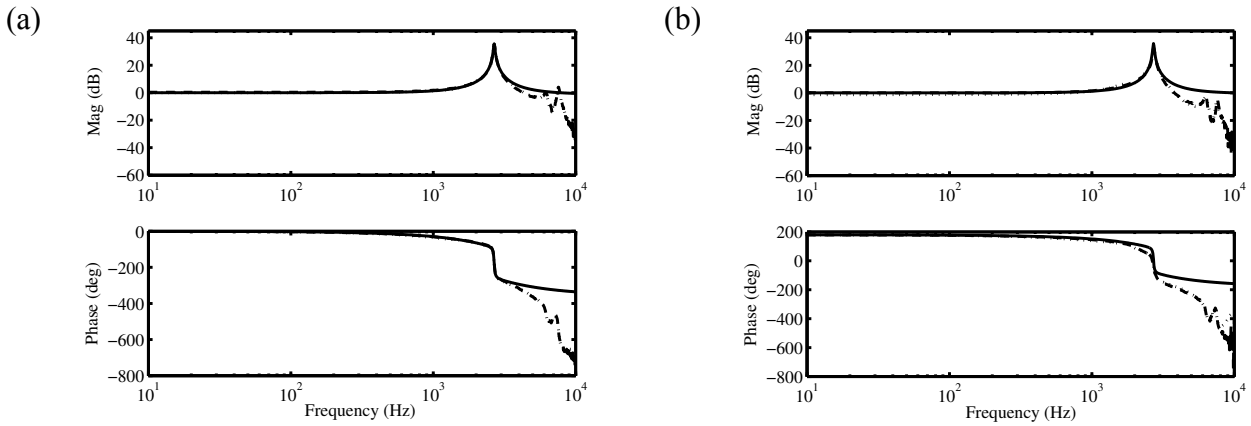

Figure 11. Frequency responses of the measured (- -), the high order (..) and the 2nd-order (-) models of the nanopositioning stage. (a) Frequency responses of the X-axis. (b) Frequency responses of the Y-axis.

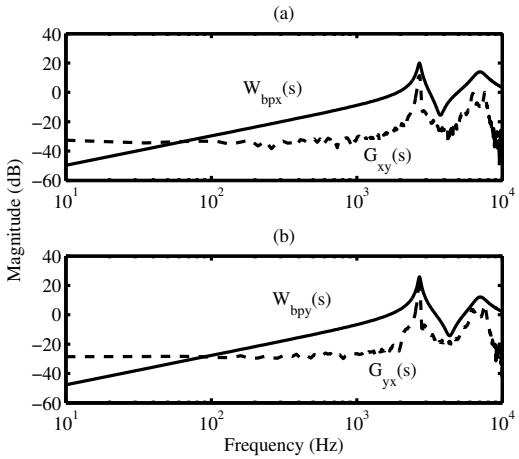

Figure 12. Weighting functions incorporated into the H∞ control design for cross-coupling attenuation. (a) W_{bpx} (-) is tuned to the resonance frequencies of G_{xy} (- -). (b) W_{bpy} (-) is tuned to the resonance frequencies of G_{yx} (- -).

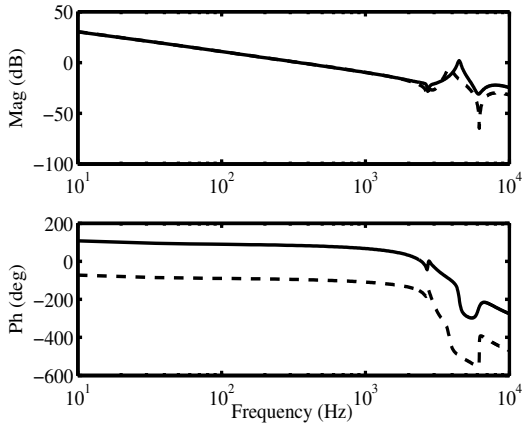

Figure 13. Frequency responses of the controllers K_x (- -) and K_y (-).

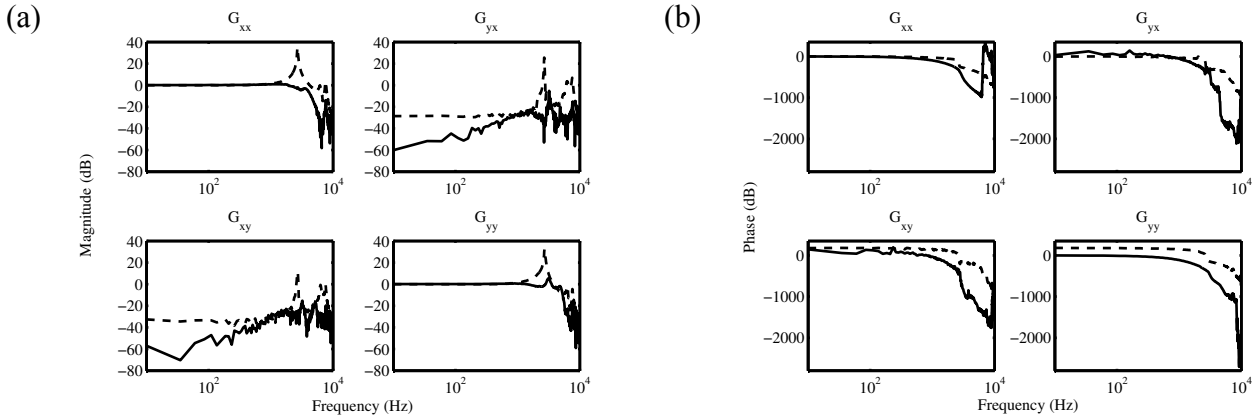

Figure 14. Measured frequency responses showing (a) magnitude (in dB), and (b) phase (in degree) of the open loop (- -) and closed loop systems with (-). The effect of cross-coupling is substantially reduced in closed loop.

Measured open and closed loop frequency responses of the nanopositioning stage are shown in Figure 14. The implemented controller attenuates the cross-coupling effect substantially. It also achieved significant damping of the resonant modes of the nanopositioner.

6. CLOSED LOOP RASTER SCANS

To evaluate the performance of the closed loop system in following raster patterns at high

speeds, triangular waves with fundamental frequencies of 40Hz, 60Hz and 100Hz were used to drive the X-axis actuator and the corresponding synchronized staircase signals were used to drive the Y-axis actuator. Figure 15 shows the desired and the actual traces of the X- and Y-axes trajectories in closed loop. It can be observed that the damping introduced by the controller has a substantial effect on the quality of the scan. The resonant modes of the stage were significantly attenuated. Therefore, the harmonics of the triangular signals do not get amplified. Another important contributor to this high quality scan is the significant closed loop attenuation of cross-coupling between the two axes of the nanopositioner at low frequencies. Furthermore due to control action the effects of piezoelectric creep and thermal drift are substantially reduced.

Comparing the closed loop raster pattern in Figure 16 with the open loop raster pattern in Figure 8, a significant improvement can be observed as a result of control action. To appreciate the improvement that has been achieved, the RMS errors corresponding to the open- and closed loop scans for 90% of the scanning range (i.e. 9µm along the X-axis) are documented in Table 1. It can be observed that the RMS error for all closed loop scans remain below 5.5nm. This is much smaller than the corresponding open loop RMS tracking errors. In particular, it can be observed that by increasing the scan frequency the open loop RMS error increases substantially. However in closed loop the scan error appears to be dominated by stochastic noise that remains relatively unchanged at different scan frequencies. For the 100Hz scan, the control strategy proposed here reduces the RMS error by 19% (from 27.8nm to 5.4nm).

Table 1. RMS errors of the raster tracking performance in open- and closed loop. The errors were calculated by considering 90% of the scanning range.

	Raster signal		
RMS error (nm)	40Hz	60Hz	100Hz
Open loop	7.7	11.9	27.8
Closed loop	5.0	5.1	5.4

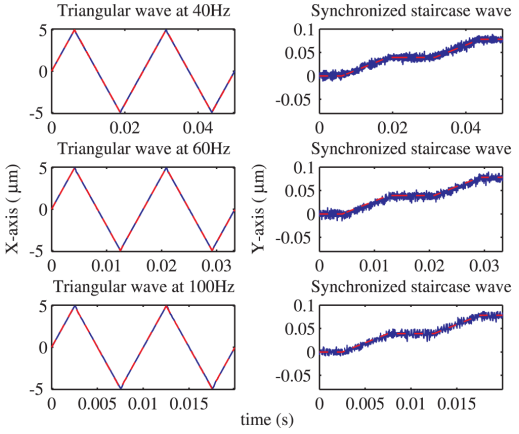

Figure 15. Closed loop tracking performance of triangular waves with fundamental frequencies of 40Hz, 60Hz and 100Hz and their corresponding synchronized staircase signals. Reference signals (- -) and output signals (-) are plotted. The effects of cross-coupling, piezoelectric creep and thermal drift are substantially reduced.

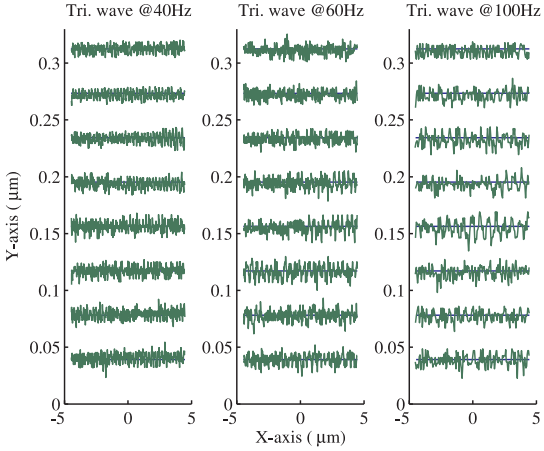

Figure 16. Closed loop raster scan results. Reference signals (- -) and output signals (-) are plotted. 90% of the scanning range which corresponds to ±4.5µm along the X-axis is plotted. The scanning lines are 39nm apart. The inclination of scan lines due to piezoelectric creep and thermal drift in the open loop system are eliminated. The cross-coupling effect is substantially reduced.

7. NOISE CHARACTERIZATION AND ESTIMATION OF RESOLUTION

One of the complications with operating nanopositioning systems in closed loop is the presence of sensor noise. Very often a nanopositioner is required to operate with a precision that is compatible to the noise level experienced by its displacement sensor [16]. This is one of the main reasons why many practitioners prefer to operate nanopositioning platforms in open loop. However,

as illustrated so far operating nanopositioning device at high speeds and in open loop is not practical. Furthermore, although low frequency operation of a nanopositioner is possible, without a feedback controller issues such as piezoelectric creep and thermal drift can not be addressed in a satisfactory manner.

In the nanopositioning framework proposed here, the resolution of the closed loop system is limited by the capacitive sensor noise. Motions of the nanopositioner that are below the sensor noise level cannot be detected, i.e. the "actual" output of the stage is not detectable at all times. In order to obtain a quantitative value of the "actual" output, the noise characterization techniques used in [34] and [16] were employed. The open loop sensor noise was measured when the stage was stationary. The noise data was then fed into a model of the closed loop system* to obtain the projected displacement of the nanopositioner. Figure 17 shows that standard deviation of the projected closed loop displacement is smaller than that of the measured open loop motion. This confirms that the "actual" output of the controlled nanopositioner is less noisy than the observed output. Based on this conclusion the scanning resolution of the platform can be improved by at least a factor of 2, allowing for a total of 512 lines scan. This amounts to 19.5nm distance between every two consecutive scan lines along the Y-axis.

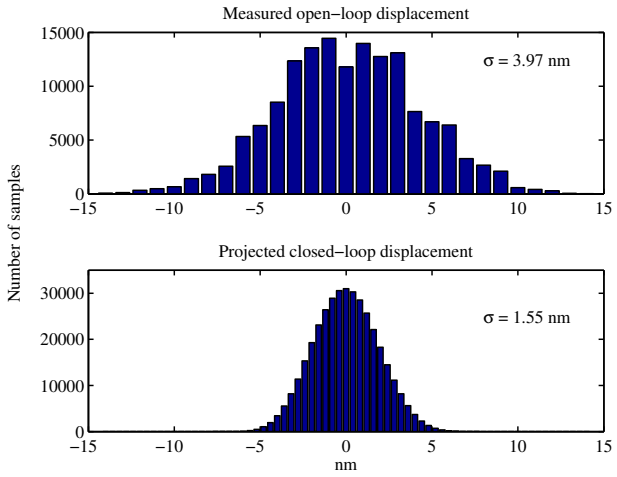

Figure 17. Measured displacements of the open loop system (top) and projected displacements of the closed loop system (bottom). The standard deviation shows that the projected closed loop output is less noisy than the observed output.

8. CONCLUSIONS

The main goal of this paper was to build a fast nanoscale positioning platform which has minima cross-coupling effects for high speed atomic force microscopy. This was done by: (a) designing a flexure-based nanopositioning device, and (b) designing and implementing a controller to minimize the positioning error arising from cross-couplings between the two axes of the stage. It was shown that fast operation of the device in open loop is not possible. The main complicating factor was identified to be the cross-coupling that exists between the two axes of the nanopositioner. Other contributors to positioning error were found to be piezoelectric creep and thermal drift. A H_∞ controller was designed to minimize the effect of resonant modes of the nanopositioner on tracking high speed raster signals. This was achieved by adding substantial damping to lightly damped poles of the system. Furthermore, real time implementation of the controller resulted in the removal of the adverse effects of thermal drift and piezoelectric creep on the generated raster patterns. Experimental raster scans over an area of 10μm×10μm, with a resolution of 39nm, at 40Hz, 60Hz and 100Hz scan frequencies demonstrated a significant improvement due to the presence of feedback controller. The

* The closed loop model is identified using the subspace based modeling technique from the measured closed loop FRF.

achieved resolution allows for generation of a 256×256 AFM image. A noise analysis of the platform suggested that the resolution can be substantially increased, allowing for an image with a resolution of, at least, 512×512 pixels over the same area.

ACKNOWLEDGEMENTS

This work was supported by the Australian Research Council Center of Excellence for Complex Dynamic Systems and Control, and a University of Newcastle ECR grant. The research was performed at the Laboratory for Dynamics and Control of Nanosystems at the University of Newcastle.

REFERENCES

1. Binnig, G., Quate, C. F., and Gerber, C., "Atomic Force Microscope," *Physical Review Letters,* Vol. 56, pp. 930-933 (1986).
2. Gonda, S., Kurosawa, T., and Tanimura, Y., "Mechanical performances of a symmetrical, monolithic three-dimensional fine-motion stage for nanometrology," *Meas. Sci. Technol.,* Vol. 10, pp. 986-993 (1999).
3. Choi, K.-B. and Lee, J. J., "Passive compliant wafer stage for single-step nano-imprint lithography," *Rev. Sci. Instrum.,* Vol. 76, pp. 075106 (2005).
4. Ando, T., Kodera, N., Uchihashi, T., Miyagi, A., Nakakita, R., Yamashita, H., and Matada, K., "High-speed Atomic Force Microscope for Capturing Dynamic Behavior of Protein Molecules at Work," *e-Journal of Surface Science and Nanotechnology,* Vol. 3, pp. 384-392 (2005).
5. Vettiger, P., Cross, G., Despont, M., Drechsler, U., Durig, U., Gotsmann, B., Haberle, W., Lantz, M. A., Rothuizen, H. E., Stutz, R., and Binnig, G. K., "The "Milipede" - Nanotechnology Entering Data Storage," *IEEE Trans. Nanotechnology,* Vol. 1, pp. 39-55 (2002).
6. Ricci, D. and Braga, P. C., "Recognizing and Avoiding Artifacts in AFM Imaging," in *Atomic Force Microscopy: Biomedical Methods and Applications*. vol. 242: Humana Press, 2004, pp. 25-37.
7. Schitter, G. and Stemmer, A., "Model-based signal conditioning for high-speed atomic force and friction force microscopy," *Microelectronic Engineering,* Vol. 67-68, pp. 938-944 (2003).
8. Sun, Y. and Pang, J. H. L., "AFM image reconstruction for deformation measurements by digital image correlation," *Nanotechnology,* Vol. 17, pp. 933-939 (2006).
9. El Rifai, O. M. and Youcef-Toumi, K., "Coupling in Piezoelectric Tube Scanners Used in Scanning Probe Microscopes," in *Proceedings of the American Control Conference, Arlington, VA*, 2001.
10. Garnaes, J., Nielsen, L., Dirscherl, K., Jorgensen, J. F., Rasmussen, J. B., Lindelof, P. E., and Sorensen, C. B., "Two-dimensional nanometer-scale calibration based on one-dimensional gratings," *Applied Physics A,* Vol. 66, pp. S831-S835 (1998).
11. Tien, S., Zou, Q., and Devasia, S., "Iterative Control of Dynamics-Coupling-Caused Errors in Piezoscanners During High-Speed AFM Operation," *IEEE Trans. Contr. Syst. Tech.,* Vol. 13, pp. 921-931 (2005).
12. Tian, X., Xi, N., Dong, Z., and Wang, Y., "System errors quantitative analysis of sample-scanning AFM," *Ultramicroscopy,* Vol. 105, pp. 336-342 (2005).
13. Bhikkaji, B., Ratnam, M., and Moheimani, S. O. R., "PVPF control of piezoelectric tube scanners," *Sensors and Actuators A,* Vol. 135, pp. 700-712 (2007).
14. Moheimani, S. O. R., "Invited Review Article: Accurate and Fast Nanopositioning with Piezoelectric Tube Scanners: Emerging Trends and Future Challenges," *Review of Scientific Instruments,* Vol. 79, pp. 071101 (2008).
15. Yong, Y. K., Aphale, S. S., and Moheimani, S. O. R., "Modeling, Design and Control of a Fast Nanopositioning Stage," *IEEE/ASME International Conference on Advanced Intelligent*

Mechatronics, (2008).
16. Aphale, S. S., Bhikkaji, B., and Moheimani, S. O. R., "Minimizing scanning errors in piezoelectric stack-actuated nanopositioning platforms," *IEEE Trans. Nanotechnology,* Vol. 7, pp. 79-90 (2008).
17. Salapaka, S., Sebastian, A., Cleveland, J. P., and Salapaka, M. V., "High bandwidth nano-positioner: A robust control approach," *Rev. Sci. Instrum.,* Vol. 73, pp. 3232-3241 (2002).
18. Ando, T., Kodera, N., Maruyama, D., Takai, E., Saito, K., and Toda, A., "A high-speed atomic force microscope for studying biological macromolecules in action," *Japanese Journal of Applied Physics,* Vol. 41, pp. 4851-4856 (2002).
19. Kwon, J., Hong, J., Kim, Y.-S., Lee, D.-Y., Lee, K., Lee, S.-m., and Park, S.-i., "Atomic force microscope with improved scan accuracy, scan speed, and optical vision," *Rev. Sci. Instrum.,* Vol. 74, pp. 4378-4383 (2003).
20. Aphale, S. S., Devasia, S., and Moheimani, S. O. R., "High-bandwidth control of a piezoelectric nanopositioning stage in the present of plant uncertainties," *Nanotechnology,* Vol. 19, pp. 125503 (2008).
21. Howell, L. L., *Compliant Mechanisms*: John Wiley & Sons, Inc. (2001).
22. Yong, Y. K., Lu, T.-F., and Handley, D. C., "Review of circular flexure hinge design equations and derivation of empirical formulations," *Precision Engineering,* Vol. 32, pp. 63-70 (2008).
23. Yong, Y. K. and Lu, T.-F., "The effect of the accuracies of flexure hinge equations on the output compliances of planar micro-motion stages," *Mechanism and Machine Theory,* Vol. 43, pp. 347-363 (2008).
24. Kindt, J. H., Fantner, G. E., Cutroni, J. A., and Hansma, P. K., "Rigid design of fast scanning probe microscopes using finite element analysis," *Ultramicroscopy,* Vol. 100, pp. 259-265 (2004).
25. Ho, K. H., Newman, S. T., S., R., and Allen, R. D., "State of the art in wire electrical discharge machining (WEDM)," *International Journal of Machine Tools and Manufacture,* Vol. 44, pp. 1247-1259 (2004).
26. Mokaberi, B. and Requicha, A. A. G., "Compensation of Scanner Creep and Hysteresis for AFM Nanomanipulation," *IEEE Trans. on Automation Science and Engineering,* Vol. 5, pp. 197-206 (2008).
27. Croft, D., Shedd, G., and Devasia, S., "Creep, Hysteresis, and Vibration Compensation for. Piezoactuators: Atomic Force Microscopy Application," *Journal of Dynamic Systems, Measurement, and Control,* Vol. 123, pp. 35-43 (2001).
28. Fleming, A. J. and Moheimani, S. O. R., "A grounded-load charge amplifier for reducing hysteresis in piezoelectric tube scanners," *Rev. Sci. Instrum.,* Vol. 76, pp. 073707 (2005).
29. Fleming, A. J. and Moheimani, S. O. R., "Sensorless vibration suppression and scan compensation for piezoelectric tube nanopositioners," *IEEE Trans. Contr. Syst. Tech.,* Vol. 14, pp. 33-44 (2006).
30. Fleming, A. J. and Moheimani, S. O. R., "Adaptive piezoelectric shunt damping," *Smart Materials and Structures,* Vol. 12, pp. 18 - 28 (2003).
31. Georgiou, H. M. S. and Mrad, R. B., "Dynamic electromechanical drift model for PZT," *Mechatronics,* Vol. 18, pp. 81-89 (2008).
32. Mokaber, B. and Requicha, A. A. G., "Drift Compensation for Automatic Nanomanipulation With Scanning Probe Microscopes," *IEEE Trans. on Automation Science and Engineering,* Vol. 3, pp. 199-207 (2006).
33. McKelvey, T., Akcay, H., and Ljung, L., "Subspace based multivariable system identification from frequency response data," *IEEE Trans. on Automatic Control,* Vol. 41, pp. 960-978 (1996).
34. Sebastian, A. and Salapaka, S. M., "Design Methodologies for Robust Nano-Positioning," *IEEE Trans. Contr. Syst. Tech.,* Vol. 13, pp. 868-876 (2005).